Basrah Journal for Engineering Sciences, Vol. 24, No. 1, (2024), 1-11

Original Article

Journal homepage: www.bjes.edu.iq
ISSN (Online): 23118385, ISSN (Print): 18146120

Mechanical Characteristic and Energy Absorption Behavior of Closed-Cell Pure and A356 Alloyed Aluminum Foams during Compression

Hayder A. Fadhil [1, *], Rafil M. Laftah [2], Qussay T. Abdulwahab [3]

[1,2,3] *Department of Mechanical Engineering, College of Engineering, University of Basrah, Basrah, Iraq*
E-mail addresses: haiderali1974@yahoo.com , rafil.laftah@uobasrah.edu.iq , qusai.abdulwahab@uobasrah.edu.iq
Received: 3 May 2023; Revised: 12 August 2023; Accepted: 24 August 2023; Published: 15 February 2024

Abstract

The goal of this study is to evaluate the mechanical characteristics and energy absorption capabilities of both closed-cell pure Aluminum foam and closed-cell A356 foam. A portion of the lightweight pure foam samples (17.12, 17.77 and 15.27 g) is produced through casting of raw material (99.9 % pure aluminum) using Titanium Hydride (TiH_2) as a foaming agent, which lead to (7.5, 7 and 8) Pores Per Inches (PPI); and samples of A356 foam (38.24, 38.18 and 35.88 g) is produced through casting of A356 alloyed material with same procedure which lead to (11, 10 and 12) PPI. In order to determine the maximum compressive strength, strength-to-weight ratio, energy absorption density, complementary energy, and energy absorption efficiency, a uniaxial compression test is conducted. The results indicate that compression of pure foam structure smashed in a ductile manner and shows a lamellar eutectic structure while A365 foams under compression are crashed with brittle character with complex phases distribution inside (polyhedral and globular morphologies), A noticeable enhancement is observed in the mechanical characteristics of the A356 foam. The maximum compressive strength and specific energy absorption of alloyed foam are increased by a factor nearly of 4 and 2 respectively for all tested samples. Also, the result shows a significant decreasing in compressive strength with increasing of PPI for both pure and alloyed foam. The notable enhancements in the properties of alloyed closed cell foam render these advanced materials a viable option for high-strength applications.

Keywords: Closed-cell aluminum foam, Optical metallography, Field emission scanning, Energy-Dispersive Spectrometry (EDS).

https://doi.org/10.33971/bjes.24.1.1

1. Introduction

Metal foams are a modern class of materials [1] that have a combination of interesting physical and mechanical properties like low density, high stiffness, low weight, and the capability of being adapted for a given purpose or function of properties that prove valuable in solving a host of design needs that exist today. The multifunctional performance of metal foams makes them attractive for numerous uses, including: thermal insulation, heat sinks, acoustic insulation, energy absorption devices, lightweight structural sandwich panels, and vibration damping devices [2].

The mechanical properties and strength-to-weight ratio are the most crucial characteristics of these materials, as they render them dependable for use as energy absorption materials [3].

1.1. Metal manufacturing

Production of metal foams is a very difficult task because of the simultaneous occurrence of solid, liquid and gaseous phases at different temperatures [4].

There are several procedures for Aluminum foam manufacturing. Banhart (2003) [2] studied three different procedures; these are Foaming Melts by Gas Injection, Foaming Melts with Blowing Agents and Solid–Gas Eutectic Solidification. Then he listed the application of the foams.

On the other hand, Rajak et al. (2017) [5] highlighted the manufacturing process of nine procedures and the properties of the produced metal foams as well as their advantages and limitations.

To find the best suitable method for Aluminum metal foams production, Mahadiv et al. (2018) [4] studied various possible methods for mechanical application. However, their experimental results showed that aluminum metal foams produced by the Powder Metallurgy method present high pore connectivity.

In their 2016 study, Nabawy et al. [6], aimed to develop a dependable manufacturing technique for various metallic foams. Pure Aluminum, Magnesium, and an Aluminum-Silicon Carbide nanocomposite (MMNC) were created through melt infiltration aided by electromagnetic force. Field Emission Scanning Electron Microscopy (FESEM) was utilized to investigate the microstructures of the resulting foam materials, which were then subjected to compression testing. The findings demonstrate that this innovative technique is highly applicable for producing metallic foams composed of pure metals and metal matrix nanocomposites.

1.2. Mechanical properties

The research from past few decades indicated that the mechanical properties capabilities of metal foams are promising fields, including: thermal insulation, heat sinks,

acoustic insulation, energy absorption devices (crash protection), lightweight structural sandwich panels (as the core material) and vibration damping devices [3].

Koza et al. (2003) [7] studied the compressive strength of Aluminum foam manufactured under powder metallurgy technique for different porosities (different density) and size, his results shown that the mean compressive strength increases almost linearly with increasing density, and the specimens having lower density exhibit steadier properties.

The mechanical properties, including stiffness, yield strength, and fracture resistance, of three commercially available closed-cell Aluminum foam types (ALPORAS, ALCAN, and ALULIGHT) were investigated for tension and compression tests by Sugimura et al. in 1997 [8]. Optical characterization of cell morphology was carried out through electro-discharge machining (EDM) and polishing, while microstructural cell characteristics were obtained through etching. The study revealed that fracture measurements indicated crack growth along cell walls via a mechanism similar to the plastic tearing of thin sheets.

In 2013, Negi et al. [9] aimed to enhance the compressive strength of Aluminum foam prepared through the melt route method by incorporating different nickel particles. The compression test results were compared with pure Aluminum foam samples to assess the impact of nickel particle percentage on the compressive strength of Aluminum foam. The stress-strain diagrams generated during the compression test were used to determine the energy absorption of various Aluminum foam samples. The compression strength test revealed that the yield strength of pure Aluminum foam was relatively low, but with the addition of nickel particles, there was a notable increase in its value. It was observed that the yield strength initially increased rapidly, but as the amount of nickel increased, the growth rate decreased, indicating that the addition of a higher percentage of nickel particles was making the foam more brittle. The incorporation of Ni elements prominently improved the plateau region compressive strength and yield stress of the foams, but to ensure ductile deformation, the content of Ni elements needed to be limited.

Gibson (2000) [10], provided a comprehensive summary of the elastic moduli, uniaxial strength, yield criterion, creep, and fatigue of metallic foams. The purpose was to establish a foundation for their potential use in engineering applications.

Motaz and Pippan (2002) [11] Standard fracture toughness tests were applied to aluminum alloy foams with different densities and in situ tests scanning electron microscope were performed to identify fracture processes and to make local deformation measurements. Fracture toughness values in terms of the critical stress intensity factor, KIC, the critical J-integral, JIC, and the critical crack-tip opening displacement, were determined.

The research is aimed to study the plastic deformation of closed-cell aluminum foam under uniaxial compression by microstructural investigation for closed cell pure aluminum and alloyed (A356) aluminum foam for a foam manufactured in "foaming melts with blowing agents" process.

For a successful design with these materials, the mechanical properties of the metal foam have to be known, and for that purpose a uniaxial compression test according to ASTM-E9 mechanical tests and microstructure investigation before and after the compression test have been done.

To get a better understanding of foam fracture, optical metallography and field emission scanning electron Microscope (FESEM) investigation have been included in the microstructure investigations.

2. Manufacturing method

A pure and alloyed closed-cell aluminum foam was produced based on addition of foaming agent in melt injection to investigate the effect of PPI on mechanical and energy absorption properties of these metals foam. However, production of metal foams is a very difficult task because of the simultaneous occurrence of solid, liquid and gaseous phases at different temperatures.

In the present work, foam is produced through casting of pure and alloyed aluminum with a chemical composition measured by a Ametex spectro material analyzer and presented in Table 1 and Table 2 was used as the raw material for closed-cell foam. Liquid-state processing is conducted using Titanium Hydride (TiH_2) as a foaming agent. Pure/alloyed aluminum is melted in carbon steel crucible and maintained at 700 ℃. 1.5 wt % calcium (as a thickening agent) in form of granules is added to the melt at a speed of 450 rpm for 10 min. 0.5 wt % of a blowing agent (TiH_2) is added in the next step at a stirring speed of 1400 rpm for 100 sec which is then poured into a cubic steel crucible in an electric furnace. Titanium hydride release hydrogen gas inside the hot viscous liquid. Foam formation occurs at 660 ℃ during 7 min. When foaming is completed, the melt is cooled and solidified, preventing hydrogen gas from escaping.

Table 1. Chemical composition of Pure Aluminum.

Si	**Fe**	**Cu**	**Mn**	**Mg**	**Zn**	**Cr**	**Ni**	**Ti**	**Be**	**Ca**	**Li**
0.04	0.12	Trace	Trace	<0.005	0.008	Trace	0.009	Trace	None	0.002	None
Pb	**Sn**	**Sr**	**V**	**Na**	**Bi**	**Zr**	**B**	**Ga**	**Al**		
Trace	<0.002	None	0.002	Trace	<0.003	Trace	0.0009	0.01	Base		

Table 2. Chemical composition of A356 alloy.

Si	**Fe**	**Cu**	**Mn**	**Mg**	**Zn**	**Cr**	**Ni**	**Ti**	**Be**	**Ca**	**Li**
6.62	0.15	0.24	0.08	<0.33	0.008	0.001		0.07			
Pb	**Sn**	**Sr**	**V**	**Na**	**Bi**	**Zr**	**B**	**Ga**	**Al**		
0.005									Base		

Blocks of solidified foams (Fig. 1) are cut using specially saw. Cutting is performed in all 6 faces in order to take the sound foam out. It should be noted that the upper surface is rather wavy due to the movements on the surface at the initial stage of casting. The lower part, on the other hand, possesses a dense structure and needs to be cut before being used. Then three samples with dimensions of 25 × 25 × 50 mm cut and prepared for compression test for both pure and alloyed foam.

Fig. 1 As cast foam block.

3. Uniaxial compression test

The compressive behavior of pure and alloyed closed-cell aluminum foam was evaluated using a compression test designed according to ASTM E8 standard [12]. The test determined the first maximum compressive strength as the yield stress. The pure/alloyed foam samples, with dimensions of 25x25x50 mm, were subjected to a uniaxial compression test using an Instron machine with a 5-ton capacity at a strain rate of 10 mm/min and at room temperature. The compression process was graphically presented in the results. The displacement-force curve was used to derive a stress-strain curve. Prior to plastic deformation, SEM images of the pure and alloyed foams were taken using a field-emission electron microscope (FESEM) with a resolution up to 20 nm at 15 kV. The morphological assessment was done according to ASTM E883-11 using different magnifications.

4. Results and discussion

4.1. Compressive behaviour and fracture mechanism

As shown in Fig. 2-a for pure and 2-b for A356 closed-cell aluminium foam, under uniaxial loading, cell walls are crushed. Work hardening of pure and alloyed samples are totally different. More stress fluctuations are observed in the case of A356 material (Fig. 2-b) and within the region of 18-25 % strain, a large drop in stress is seen (Figs. 20 and 21). Images of the super-slow camera (Fig. 2-b) show the fact that the A356 sample is crushed and broken into several parts due to compression. This indicates the brittle nature of the material as already confirmed by SEM images. It can be concluded that A356 foam is a relatively high-strength material with pore walls breaking under compression in a brittle fashion. The process of wall failure is continuous and time consuming and results in fluctuations in stress-strain curve. Further increase in strain (up to about 45%) is a result of foam densification.

Contrary to the alloyed material, foams fabricated from pure aluminium do not show any work-hardening behaviour. A relatively linear trend in stress is seen up to 45 % of strain where the sample is smashed. Images of the sample (Fig. 2-a) reveal this behaviour. No fragmentation is observed during plastic deformation and pore walls keep their consistency through forming local hinges throughout the entire sample. Finally, the sample becomes flat like a compressed spring.

Fracture mechanisms mentioned above are already observed in SEM microstructures revealing fragmentation and smashing as main mechanisms with more crushing seen in the case of alloyed foam. This means that the A356 foam (which is 4-times stronger than pure material) has a larger energy absorption capacity as well.

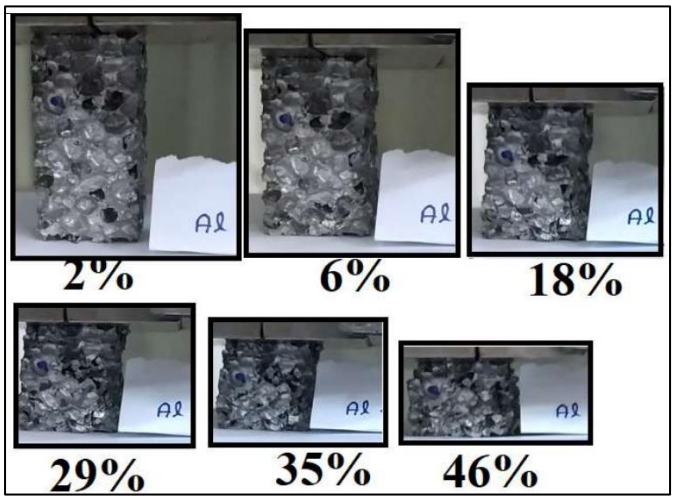

Fig. 2-a Compression behavior of Closed-cell pure Aluminum foam at a strain rate of 10 mm/min across varying stages of compression (strain).

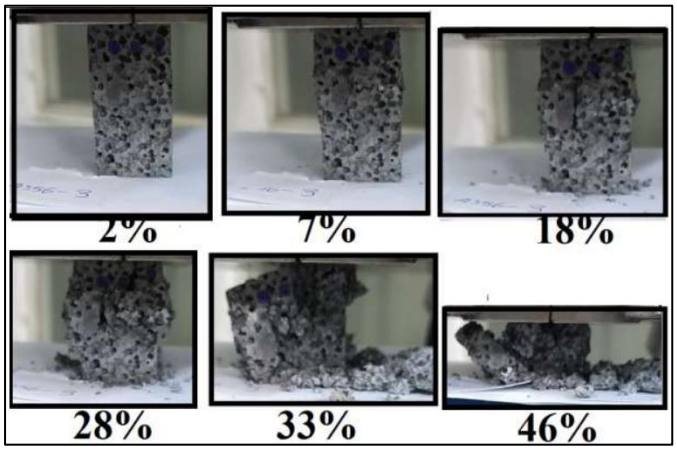

Fig. 2-b Compression behavior of closed-cell A356 Aluminium foam at a strain rate of 10 mm/min across varying stages of compression (strain).

4.2. Electron microscopy (SEM)

4.2.1. A closed-cell A356 foam

The foam appearance under FESEM is observed in Fig. 3. A uniform structure is seen in which, cell walls seem to be thicker than commercially-available foams [1]. Wall thicknesses and pore sizes are marked in Fig. 4. Wall thickness lies in the range of 250-850 microns while pores are between 2-3.5 mm in diameter.

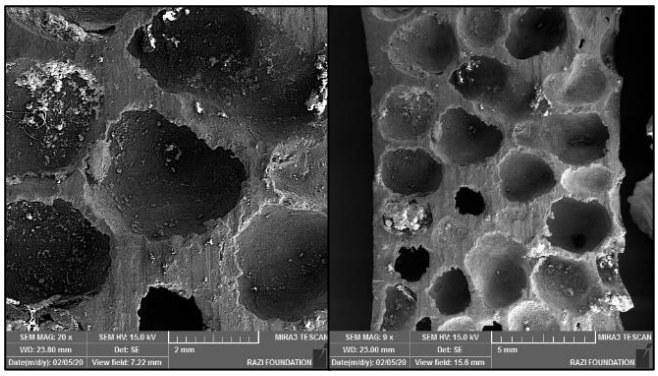

Fig. 3 A356 foam under FESEM revealing a rather uniform cell structure.

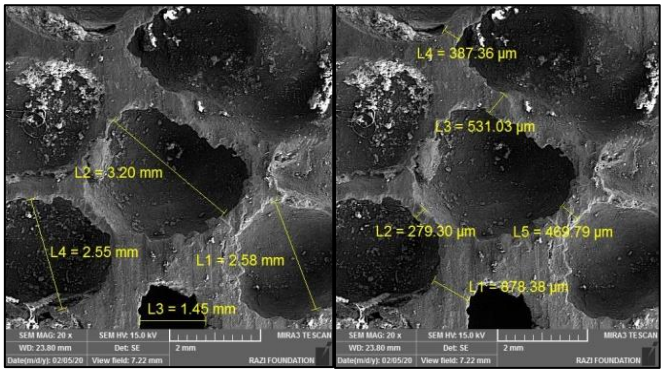

Fig. 4 (a) pore size. (b) Wall thickness for A356 foam determined under FESEM.

The elemental composition of foams was determined using energy-dispersive spectrometry (EDS) of the FESEM. For this, plateau zone (the junction between three bubbles, as well as wall ends were analysed. Magnified image of such a zone is depicted in Fig. 5.

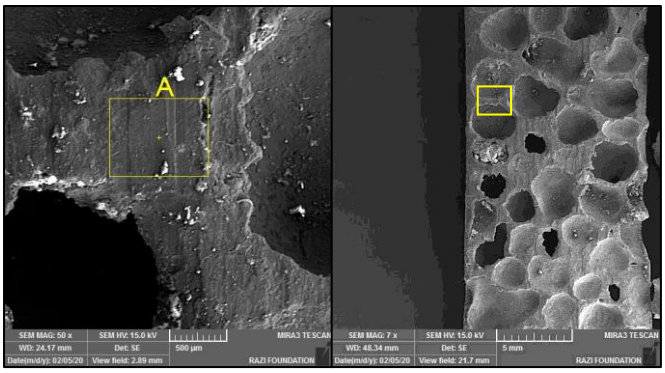

Fig. 5 Magnification of the zone selected for EDS analysis.

EDS analysis results are presented in Fig. 6. In addition to aluminium and silicon, iron was also detectable which originates from dissolution of the mixer blade in the melt. Also, calcium seems to be abundant which the result of calcium addition is during thickening. The presence of these elements will change the chemical composition of the original alloy (A356) but is a fact accepted by producers. Finally, titanium (remaining due to the addition of TiH_2 bubbler) is also detected by EDS detector (hydrogen leaves the material during bubbling).

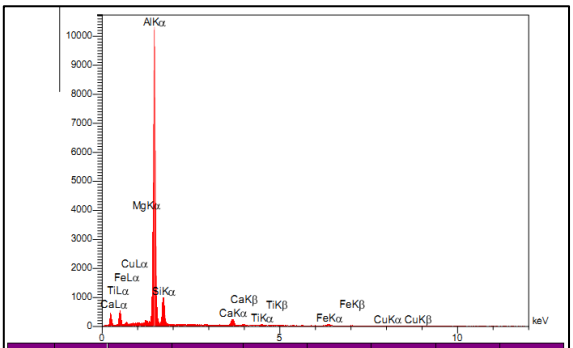

Elt	Line	Int	Error	K	Kr	W%	A%	ZAF
Mg	Ka	6.3	23.2532	0.0033	0.0029	0.31	0.36	0.9316
Al	Ka	1605.3	23.6029	0.8205	0.7237	77.28	81.03	0.9365
Si	Ka	146.8	23.9525	0.0784	0.0692	12.58	12.67	0.5501
Ca	Ka	45.6	0.3862	0.0472	0.0416	4.62	3.26	0.9001
Ti	Ka	6.5	0.3965	0.0085	0.0075	0.89	0.52	0.8481
Fe	Ka	14.8	0.3854	0.0376	0.0331	3.84	1.95	0.8626
Cu	Ka	0.9	0.2915	0.0045	0.0040	0.48	0.22	0.8260
				1.0000	0.8821	100.00	100.00	

Fig. 6 EDS analysis result for zone A marked in Fig. 5.

In addition to the triple junction (marked as zone "A" in Fig. 5), pore walls (marked as zone "B" in Fig. 7) were also examined through EDS in Figs. 7 and 8, respectively. Clearly, the amount of silicon and titanium is much higher on the surface as compared to the junction. This is a direct result of bubble nucleation by TiH_2 and floating feature of silicon. Therefore, A356 foams present a concentration gradient when moving from internal surface of the bubble to the core of the walls.

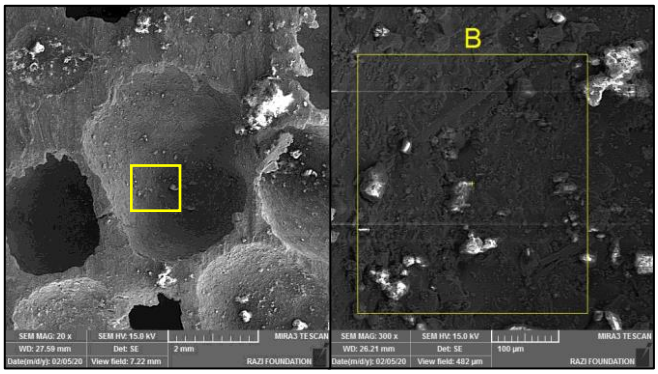

Fig. 7 Zone B selected for EDS analysis of internal pore walls.

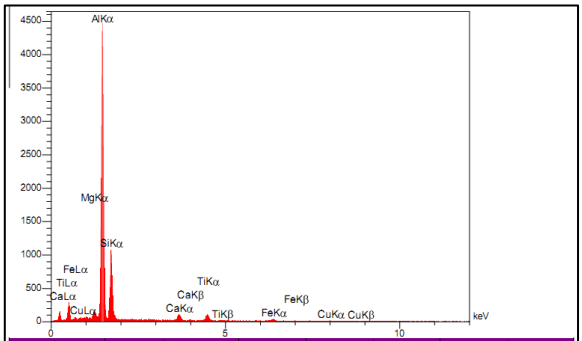

Elt	Line	Int	Error	K	Kr	W%	A%	ZAF
Mg	Ka	12.5	12.6375	0.0126	0.0105	1.17	1.39	0.8995
Al	Ka	686.4	12.8275	0.6819	0.5682	62.14	66.33	0.9144
Si	Ka	167.9	13.0175	0.1743	0.1453	24.07	24.68	0.6036
Ca	Ka	18.3	0.5524	0.0368	0.0307	3.40	2.44	0.9038
Ti	Ka	21.3	0.5673	0.0541	0.0450	5.30	3.19	0.8502
Fe	Ka	6.5	0.4744	0.0319	0.0266	3.09	1.59	0.8623
Cu	Ka	0.8	0.4428	0.0083	0.0069	0.84	0.38	0.8270
				1.0000	0.8333	100.00	100.00	

Fig. 8 EDS analysis result for zone B marked in Fig. 7.

In the next step, foams were mounted in a resin in order to be evaluated in detail under electron microscope for being compared with optical microscopy findings. Images of the sample are shown in Fig. 9 under secondary electron (SE) and backscatter (BS) conditions, thus making different phases distinguishable.

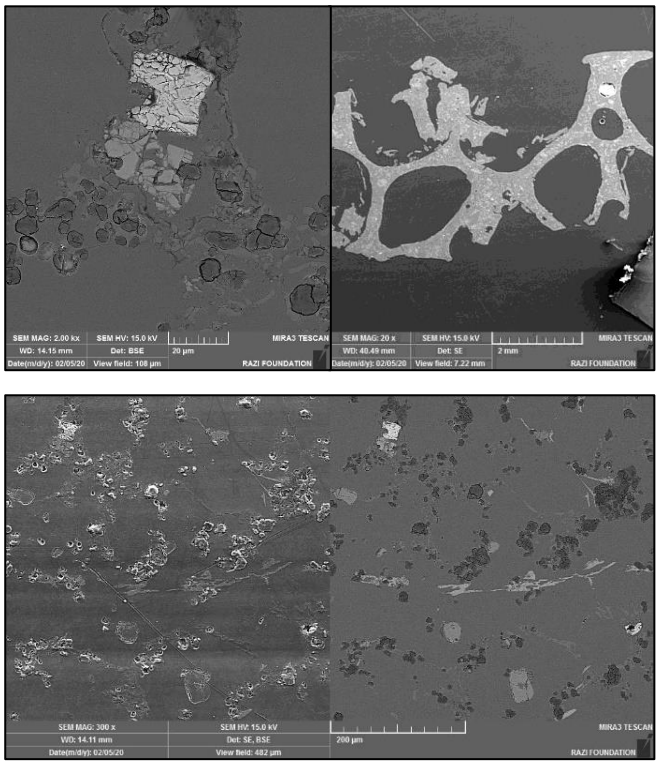

Fig. 9 FESEM micrographs of the etched A356 foam sample.

The sample was analysed through EDS mapping for a better understanding of the material under study. Results (Fig. 10) show the possibility of formation of a number of complexes such as Al-Si, Al-Cu, Fe-Al, and Al-Mg in addition to the presence of titanium. Here, Al-Si look to possess larger percentage among all.

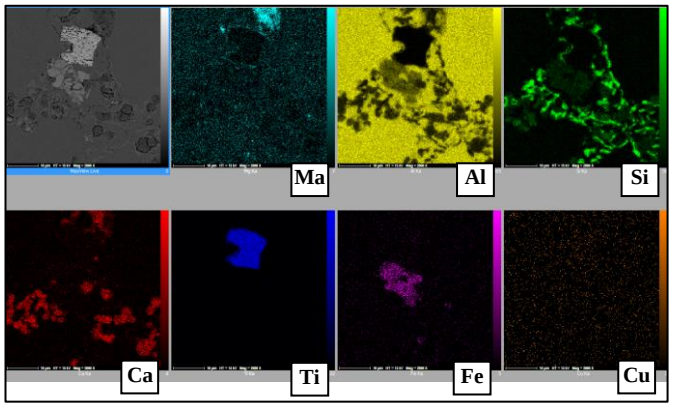

Fig. 10 Element mapping distribution of Fe, Ti, Si, Al, Mg, Cu and Ca.

4.2.2. Closed-cell pure aluminium foam

An FESEM image of pure aluminium foam is shown in Fig. 11. A rather uniform structure with thin walls is observed. In comparison to the alloyed foam, the pure material possesses larger pores with thinner walls in between. Pore dimensions and wall thicknesses are marked in the same image.

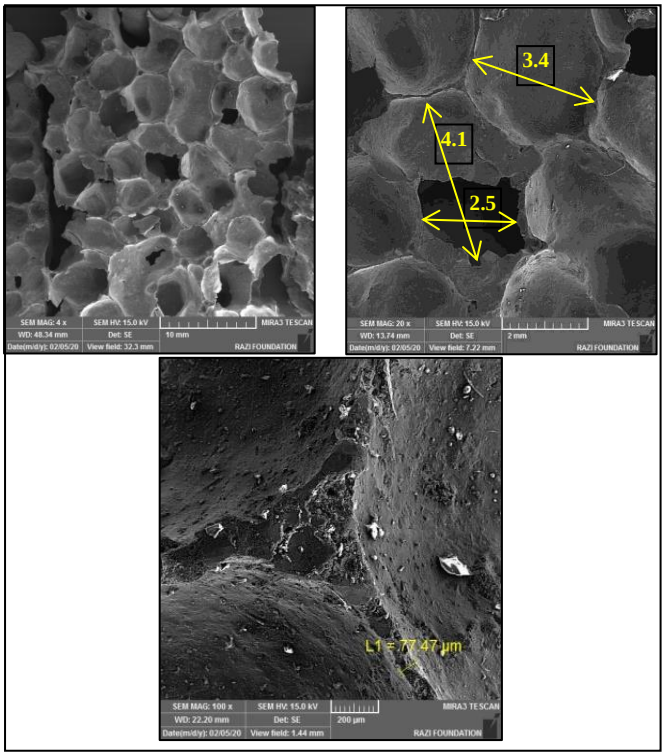

Fig. 11 Pure aluminium foam and its pore specifications.

Figure 11 clear the pore sizes lie in the range of 2.5 to 4.5 mm which are larger than the alloyed counterpart. Also, pore wall thicknesses are in the range of 50-130 microns. In other words, expansion of the pores makes the wall thinner. If reached to a critical value, they are burst. This phenomenon is already visible in microstructures. In the case of alloyed foam, however, burst structure is not observed which means that silicon affects wall formation in a positive way, making the walls thicker and more rigid during foaming. These phenomena result in a decrease in foam density with a reduced PPI. In other words, pure foam is lighter than the alloyed one. However, its strength falls below the A356 foam as presented in Fig. 20.

Similar to alloyed samples, pure foams were also analysed via EDS. The triple junction in Fig. 12 (marked as “zone A”) was tested with results presented in Fig. 13.

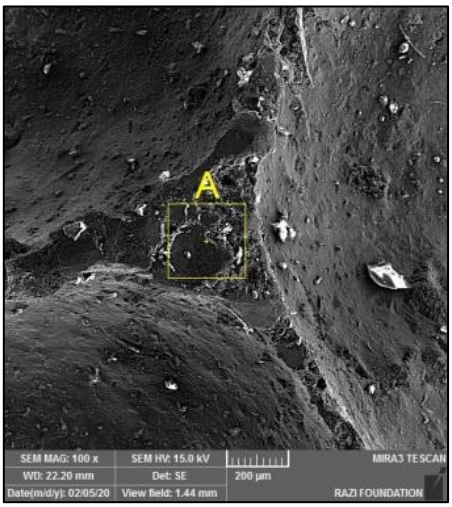

Fig. 12 EDS analysed triple junction area.

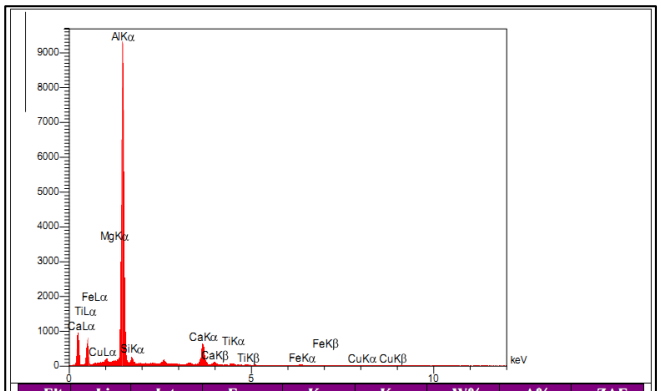

Elt	Line	Int	Error	K	Kr	W%	A%	ZAF
Mg	Ka	0.0	0.0000	0.0000	0.0000	0.00	0.00	0.9028
Al	Ka	1416.8	42.9461	0.8119	0.7420	80.55	86.38	0.9211
Si	Ka	9.0	43.5823	0.0054	0.0049	0.092	0.95	0.5371
Ca	Ka	128.9	0.5780	0.1495	0.1367	14.95	10.79	0.9138
Ti	Ka	6.2	0.5935	0.0091	0.0083	0.99	0.60	0.8396
Fe	Ka	5.6	0.5909	0.0159	0.0146	1.69	0.87	0.8628
Cu	Ka	1.4	0.9193	0.0081	0.0074	0.90	0.41	0.8289
				1.0000	0.9139	100.00	100.00	

Fig. 13 EDS analysed results for zone A marked in Fig. 12.

Again, traces of iron (remaining from mixer blade) are observed in the sample. Calcium (added for thickening) was also detected. Most probably, silicon is remained from the previous runs with alloyed material. Finally, titanium is coming from TiH_2 addition as the bubbling agent.

The interior wall of a pore (marked as "zone B") is depicted in Fig. 14 for which, EDS analysis results are brought in Fig. 15.

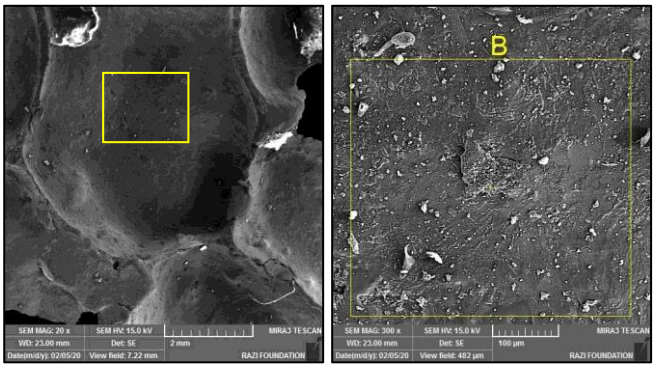

Fig. 14 EDS analysis of the internal pore walls of pure foam.

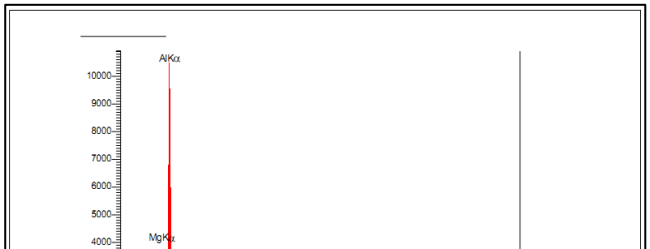

Elt	Line	Int	Error	K	Kr	W%	A%	ZAF
Mg	Ka	2.7	7.4356	0.0014	0.0013	0.15	0.17	0.9117
Al	Ka	1609.9	7.5474	0.8479	0.7787	84.28	89.55	0.9238
Si	Ka	3.2	7.6592	0.0017	0.0016	0.30	0.31	0.5239
Ca	Ka	98.8	0.3586	0.1053	0.0967	10.62	7.60	0.9107
Ti	Ka	0.6	0.3682	0.0008	0.0007	0.09	0.05	0.8462
Fe	Ka	14.9	0.4562	0.0391	0.0359	4.15	2.13	0.8646
Cu	Ka	0.7	0.2580	0.0037	0.0034	0.41	0.19	0.8288
				1.0000	0.9184	100.00	100.00	

Fig. 15 EDS analysis results of zone "B".

Figure 15 show that the concentration gradient in pure foam is lower than the alloyed A356 foam and those complexes mentioned earlier are not formed. Al-Ca eutectic alloy is the only complex remaining in after foaming which can be effective in strengthening of the material.

The foam under study was prepared through polishing and etching using Keller's reagent in order to make detailed metallographic examinations possible. Results, depicted in Fig. 16, show the microstructure under FESEM. These images are taken in SE and BSE modes in order to make the phase contrast which is clearly visible in BSE mode. Indentations in the pore walls are result of resin detachment during polishing.

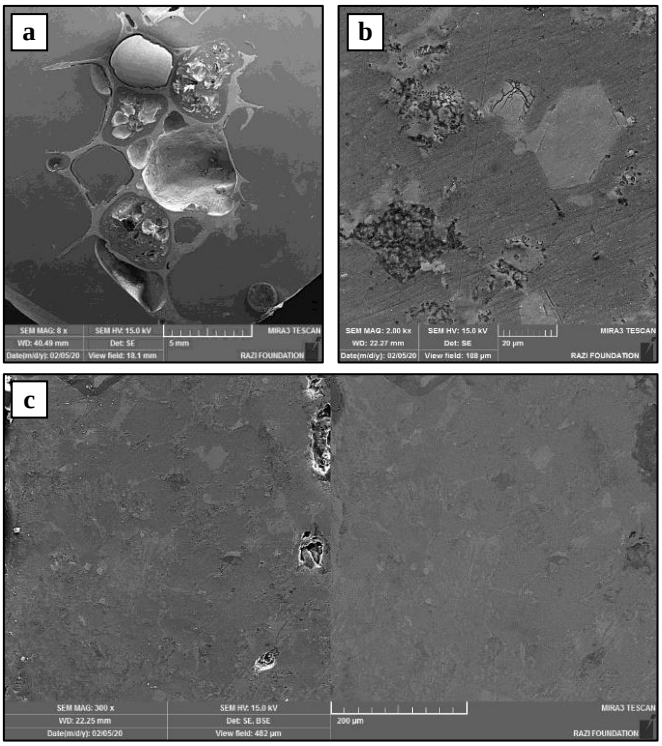

Fig. 16 (a, b) Microstructure of pure aluminium foam after etching. (c) comparison of the microstructure under SE and BSE modes.

EDS maps of the sample are provided in Fig. 17 where the addition of calcium to the melt introduces the material as an alloy (to this, one needs to add the presence of iron remained from the steel impeller). Composition maps reveal the presence of aluminium-calcium eutectic alloy. Titanium is remained from TiH_2 as foaming agent and no complex is formed in this system. The Al-Ca system decides the strength of the foam material.

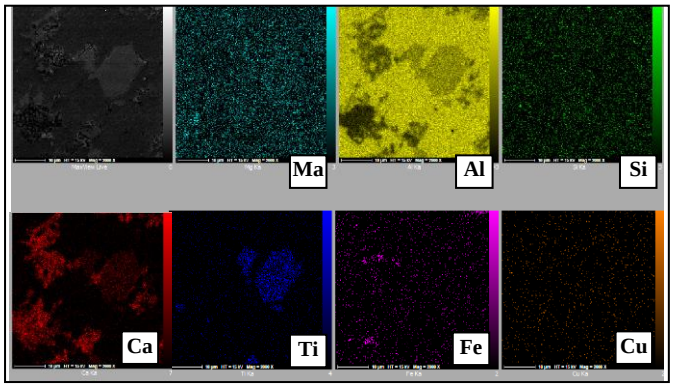

Fig. 17 Pure aluminium element mapping distribution of Fe, Ti, Si, Al, Mg, Cu and Ca.

In contrast to the alloyed material, no dispersion strengthening is expected here. Therefore, crack formation and propagation rate (during plastic deformation) is much slower than A356 foam. This is the origin of its higher strength in comparison to the alloyed A356 foam.

In simple words, foams fabricated out of pure aluminium show the tendency toward ductile behaviour whereas A356 foam is brittle and breaks down under loading. Cracks formed due to the presence of complexes and eutectic phase, render the material brittle and prone to failure.

4.2.3. Fracture cross-section after compression test

Sample residuals after uniaxial compression testing were collected and examined under FESEM in order to find out more details on fracture mode. Results are depicted in Fig. 18 for both pure and alloyed materials after being crashed under compression.

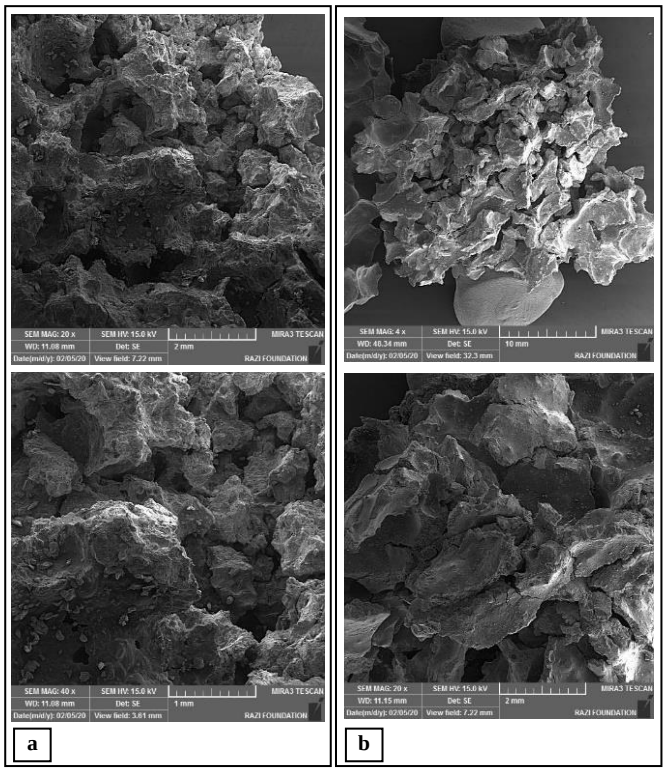

Fig. 18 Microstructure of fracture surface (a) A356, (b) pure aluminium.

Higher magnification (1500X, at 15 kV, 20 nm resolution) of the fracture surfaces (Fig. 19) reveals a brittle character for A356 with complex phases distributed inside (polyhedral and globular morphologies). No dimple (characteristic of ductile fracture) is seen. In contrast, pure aluminium foam shows a lamellar eutectic structure being quite different from the alloyed material. In other words, failure of the alloyed foam is accompanied with particle crashing and low work-hardening while in the case of pure foam, the structure fails in a ductile manner showing higher levels of work-hardening. Therefore, their stress-strain behaviour and energy absorption properties differ to a large extent.

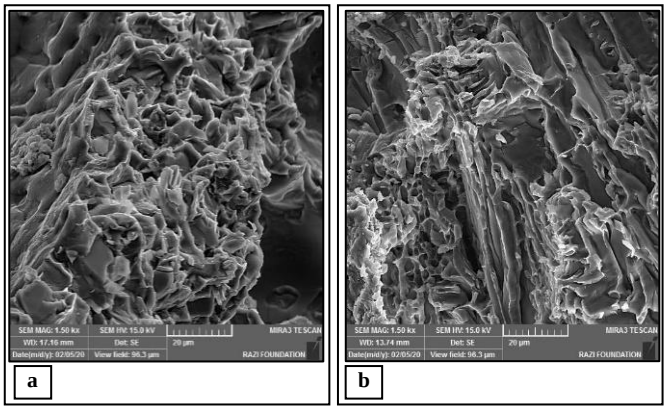

Fig. 19 Failure modes in pore walls (a) A356, (b) pure aluminium.

When alloyed, aluminium foams reveal a much stronger structure as compared to the pure material processed in the same way. This is reflected in the results of compression testing (Fig. 20) where A356 foam shows a larger area (means need to higher energy for plastic deformation).

Electron microscopy examinations confirm the difference in failure modes. While A356 behalves in a brittle manner, the pure material fails in a ductile mode. The former shows larger fracture strength whereas the latter reveals smaller fracture strength values. Therefore, A356 foam, although comes with higher density, it presents larger energy absorption capacity and strength.

Figures 20 and 21 discloses the fact that in comparison to the pure sample, alloyed foam shows higher strength under the same foaming conditions (i.e. 0.5 wt % of foaming agent and 1 wt % of Ca). This is a result of alloying and possessing needle-like Si particles.

4.3. Elastic properties

According to ISO 13 314, the yield point is one of the critical parameters of any cellular material. A stress-strain curves for three A356 and three pure foams at strain rate of 10 mm/min are disclosed in Figs. 20 and 21 respectively, shows that the yield strength of A356 foam are about 4-times yield strength as compared to the pure counterpart and increasing the PPI negatively affects the yield strength (Figs. 22 and 23) [13]. According to the idea previously mentioned in the fracture mechanism of structures to the best of our knowledge, these values are the largest values reported so far; this is probably due to the thicker pore walls compared to the commercially available products such as Alolaight and Aloporos. In addition, solid pores show a more curved morphology. These two features result in better yield strength and are seen more in alloyed foam than the pure sample (compare Figs. 4 and 11). Therefore, higher yield values for A356 foam comes from:

1. Spherical structure of the cells and their thickness.
2. Alloying and strengthening by needle-like particles.

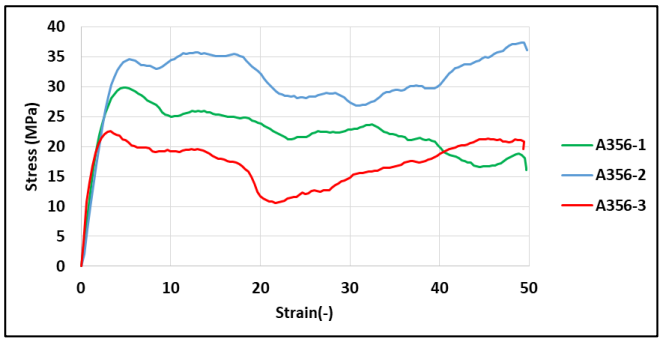

Fig. 20 Stress-strain curve for A356 closed cell aluminium foam compression test (3 samples).

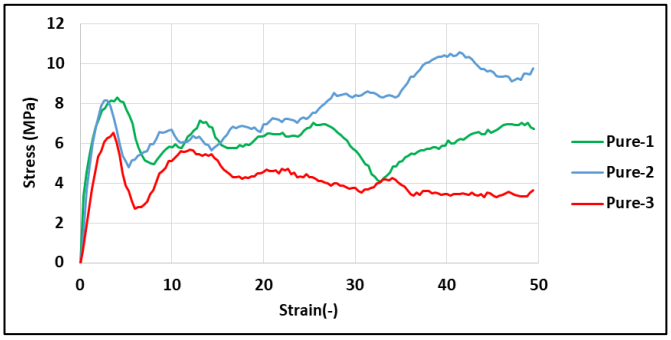

Fig. 21 Stress-strain curve for pure closed cell aluminium foam compression test (3 samples).

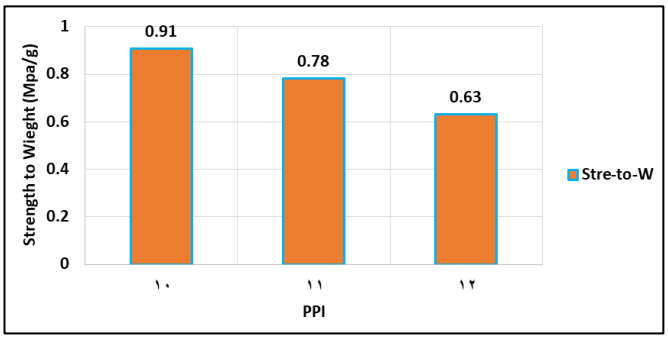

Fig. 22 strength-PPI for A356 closed cell aluminium foam compression test (3 samples).

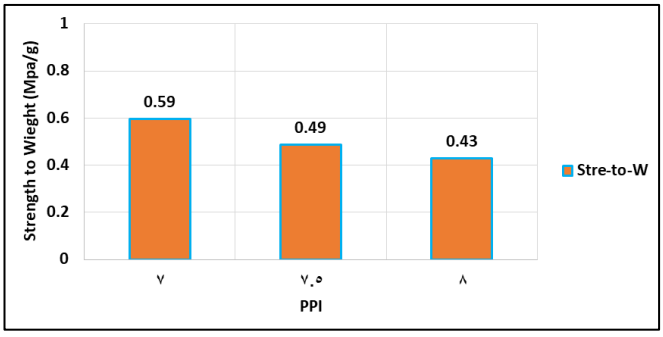

Fig. 23 strength-PPI for pure closed cell aluminium foam compression test (3 samples).

4.4. Properties of energy absorption

The examined properties of the foam samples in this study include absorbed energy density, complementary energy, total energy, specific energy absorption, energy absorption efficiency, and energetic behaviors at different stress levels. The relationship between normalized energy and stress and the impact of pores per inch (PPI) on energy absorption are also analyzed and compared.

4.5. Total energy

The energy absorbed by the material can be divided into two parts: The energy absorbed per unit volume, which is also referred to as the energy absorption density or strain energy, comprises the first part. The second part is the complementary energy. Equations (1) and (2) are used to calculate these values, as shown in the schematic in Fig. 24. The total energy absorbed can be calculated using Equation (3) [14].

$$u = \frac{U}{V} = \int_0^x \frac{F\,dx}{V} = \int_0^x \frac{F\,dx}{A\,X_0} = \int_0^\varepsilon \sigma\,d\varepsilon \tag{1}$$

$$u^* = \frac{U^*}{V} = \int_0^F \frac{x\,dF}{V} = \int_0^F \frac{x\,dF}{A\,X_0} = \int_0^\sigma \varepsilon\,d\sigma \tag{2}$$

$$u_t = u + u^* = \int d(\sigma\,\varepsilon) = \int \sigma\,d\varepsilon + \int \varepsilon\,d\sigma \tag{3}$$

in which; u_t: total energy, V: foams volume and the other parameters are explained in Fig. 24.

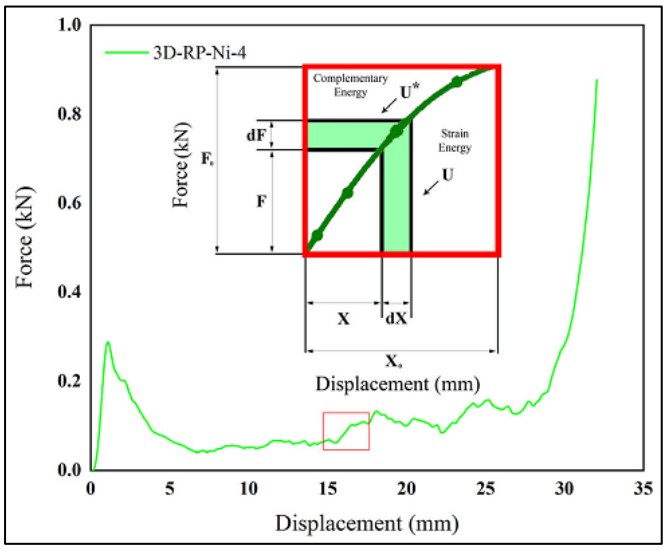

Fig. 24 approach for computing the total energy.

The energy absorption density of A356 foam and pure foam (strain energy) is calculated by Equation (1) and presented comparatively in Figs. 25-a and 26-a respectively. As the strain increases, the quantity of absorbed energy also increases. It is also slightly related PPI for pure foam and more affected by PPI changes for A356 foam, and it is evident that structures with higher density absorb greater amounts of energy at equivalent strains.

Figures 27 and 28 show, alloyed foam absorbed maximum energy 0.06, 0.08 and 0.12 (MJ m-3) for PPI 10, 11, and 12, while for pure foam 0.014, 0.022 and 0.031 (MJ m-3) for PPI 7, 7.5, and 8, respectively.

It is noteworthy to compare the energy absorption density of pure foam related to PPI and alloyed foam, the increased PPI, and the Silicon improved the absorbed energy of A356 foam to 4 times compared with pure one, and that related to increasing stress increases the values of total energy absorption (Fig. 24), which leads to increasing the total energy of the core materials, as shown in Table 27 and Fig. 28.

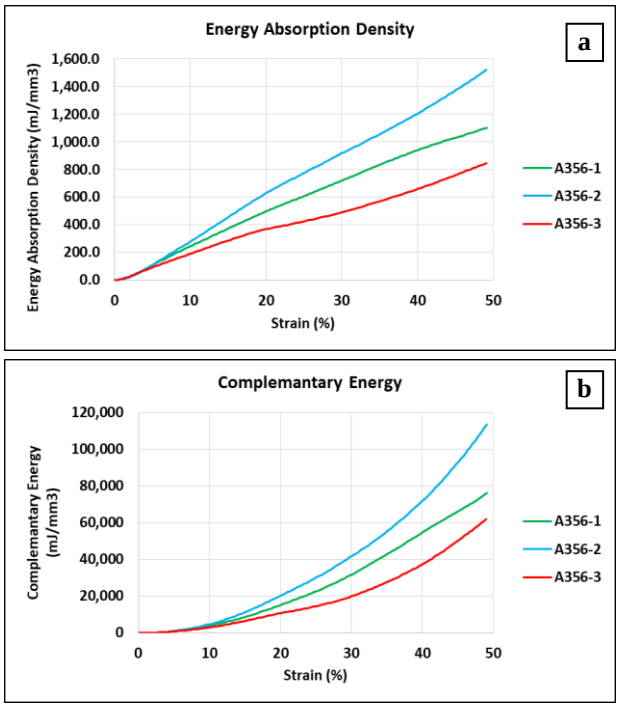

Fig. 25 (a) Energy absorption density of A356 closed-cell foam. (b) Complementary strain energy of A356 closed-cell foam.

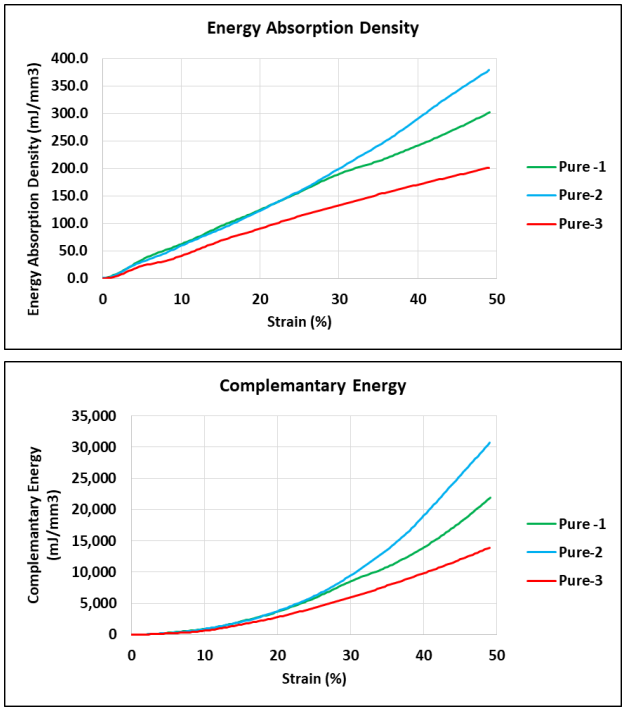

Fig. 26 (a) Energy absorption density of pure aluminum closed-cell foam. (b) Complementary strain energy of pure aluminum closed-cell foam.

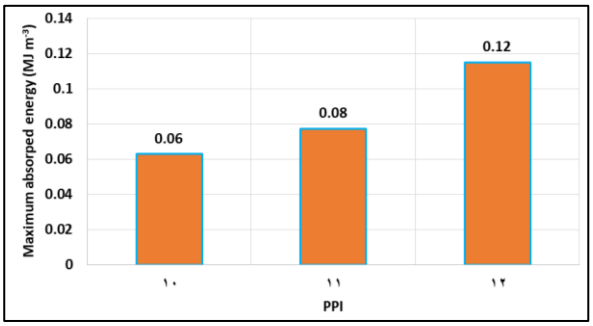

Fig. 27 Max. energy absorption density of A356 aluminum closed-cell foam related to PPI.

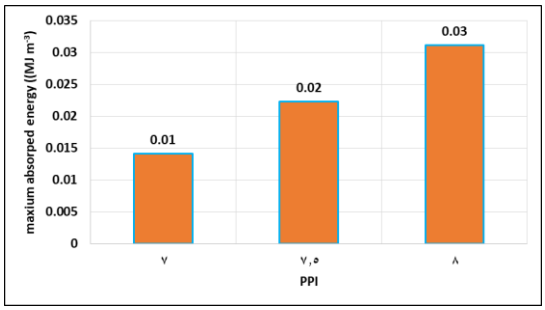

Fig. 28 Max. energy absorption density of pure aluminum closed-cell foam related to PPI.

4.6. Energy Absorption Efficiency

The rate of energy (η) absorbed at a particular strain relative to the total amount of absorbed energy and is calculated through Equation (4) [21] and is plotted concerning displacement in Figs. 29 and 30 for both alloyed and pure closed cell aluminum foam respectively.

$$\eta = \frac{1}{\sigma_m \, \varepsilon_m} \int_0^{\varepsilon_m} \sigma \, d\varepsilon \tag{4}$$

in which η is energy absorption efficiency, ε_m and σ_m is strain an stress at a certain strain εm respectively.

Based on Figs. 29 and 30, it can be observed that the alloyed and pure samples exhibit similar behavior. The energy absorption efficiency curve shows a peak and then a decrease, followed by a stable region. The peak occurs around the yield point of the samples. A365 foams have better efficiency due to their elastic nature, and their efficiency is significantly lower. These results were obtained from force-displacement diagrams and can guide material selection for industrial applications of these lightweight foams.

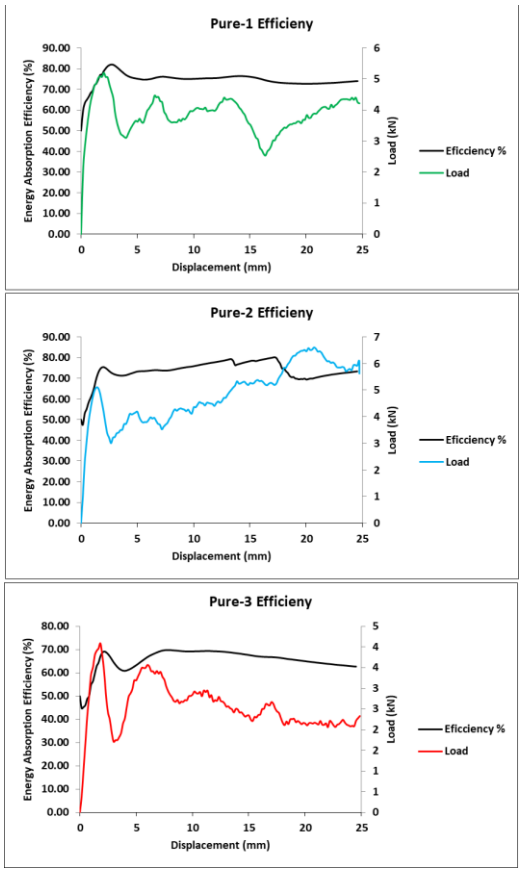

Fig. 29 Energy absorption efficiency of A356 aluminum closed-cell foam.

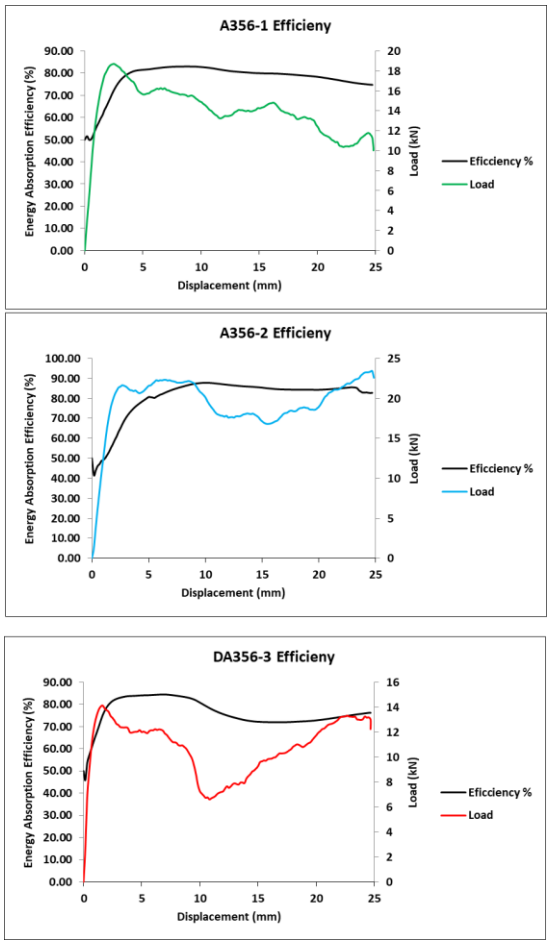

Fig. 30 Energy absorption efficiency of pure aluminum closed-cell foam.

5. Conclusions

A lightweight pure foam was produced using 99.9% pure aluminum and Titanium Hydride (TiH2) as a foaming agent, resulting in PPI values of 7, 7.5, and 8. A356 alloyed foam was also produced using the same procedure, resulting in PPI values of 10, 11, and 12.

Uniaxial compression tests results showed that compression of the pure foam structure exhibited a ductile fracture mode with a lamellar eutectic structure, while A356 foams showed a brittle fracture mode with a complex phase distribution (polyhedral and globular morphologies).

A significant improvement in the mechanical properties of A356 foam was observed, which varied with the increase in PPI.

Alloyed foam improved maximum compressive strength and specific energy absorption by 4 times and 2 times, respectively.

The results also indicated a significant decrease in compressive strength with an increase in PPI for both pure and alloyed foam. These findings demonstrate that alloyed closed-cell foam exhibits significantly improved properties, making them a suitable candidate for high-strength applications.

for A356 closed-cell aluminium foam, under uniaxial loading, cell walls are crushed. Work hardening of pure and alloyed samples are totally different. More stress fluctuations are observed in the case of A356 material and within the region of 18-25 % strain, a large drop in stress is seen. Images of the super-slow camera show the fact that the A356 sample is crushed and broken into several parts due to compression. This indicates the brittle nature of the material as already confirmed by SEM images. It can be concluded that A356 foam is a relatively high-strength material with pore walls breaking under compression in a brittle fashion. The process of wall failure is continuous and time consuming and results in fluctuations in stress-strain curve. Further increase in strain (up to about 45 %) is a result of foam densification.

Fracture mechanisms mentioned above are already observed in SEM microstructures revealing fragmentation and smashing as main mechanisms with more crushing seen in the case of alloyed foam. This means that the A356 foam (which is 4-times stronger than pure material) has a larger energy absorption capacity as well EDS analysis results are presented.

In addition to aluminum and silicon, iron was also detectable which originates from dissolution of the mixer blade in the melt. Also, calcium seems to be abundant which the result of calcium addition is during thickening. The presence of these elements will change the chemical composition of the original alloy (A356) but is a fact accepted by producers. Finally, titanium (remaining due to the addition of TiH_2 bubbler) is also detected by EDS detector (hydrogen leaves the material during bubbling).

The sample was analysed through EDS mapping for a better understanding of the material under study. Results show the possibility of formation of a number of complexes such as Al-Si, Al-Cu, Fe-Al, and Al-Mg in addition to the presence of titanium. Here, Al-Si look to possess larger percentage among all.

Electron microscopy examinations confirm the difference in failure modes. While A356 behalves in a brittle manner, the pure material fails in a ductile mode. The former shows larger fracture strength whereas the latter reveals smaller fracture strength values. Therefore, A356 foam, although comes with higher density, it presents larger energy absorption capacity and strength.

The resulting stress-strain curves discloses the fact that in comparison to the pure sample, alloyed foam shows higher strength under the same foaming conditions (i.e. 0.5 wt % of foaming agent and 1 wt % of Ca). This is a result of alloying and possessing needle-like Si particles.

The results indicate that as the strain increases, the amount of absorbed energy also increases. In pure foam, this relationship is slightly related to PPI, while in A356 foam, it is more affected by changes in PPI. Furthermore, it is evident that denser structures absorb more energy at equivalent strains.

References

[1] M. F. Ashby, A. G. Evans, N. A. Fleck, L. J. Gibson, J. W. Hutchinson and H. N. G. Wadley, Metal Foams: A Design Guide, Butterworth-Heinemann, 2000.

[2] J. Banhart, Aluminum Foams: On the Road to Real Applications, MRS Bulletin, 2003. https://doi.org/10.1557/mrs2003.83

[3] S. R. Nejad, M. Hosseinpour, S. M. H. Mirbagheri, “Investigation of energy absorption behavior of light sandwich panel with nickel/polymer open-cell foam core during compression”, Advanced engineering materials, Vol. 24, Issue 12, 2022. https://doi.org/10.1002/adem.202200663

[4] Mahadev, C. G. Sreenivasa and K. M. Shivakumar, “A Review on Production of Aluminium Metal Foams”, Sreenivasa, Materials Science and Engineering, 2018. https://doi.org/10.1088/1757-899X/376/1/012081

[5] D. K. Rajak, L. A. Kumaraswamidhas and S. Das, "Technical Overview of Aluminum Alloy Foam", Rev. Adv. Mater. Sci., Vol. 48, pp. 68-86, 2017.
[6] A. M. Nabawy, K. A. Khalil, A. M. Al-Ahmari, El. M. Sherif, "Melt Processing and Characterization of Al-SiC Nanocomposite, Al, and Mg Foam Materials", Metals, Vol. 6, Issue 5, 2016. https://doi.org/10.3390/met6050110
[7] E. Koza, M. Leonowicz, S. Wojciechowski, F. Simancik, "Compressive strength of aluminum foam", Materials Letters, Vol. 58, Issue 1-2, pp.132 –135, 2004. https://doi.org/10.1016/S0167-577X(03)00430-0
[8] Y. Sugimura, J. Meyer, M. Y. He, H. Bart-Smith, J. Grenstedt, A. G. Evans, "On the Mechanical performance of Closed Cell Al Alloy Foams", Acta Materialia, Vol. 45, Issue 12, pp. 5245-5259, 1997. https://doi.org/10.1016/S1359-6454(97)00148-1
[9] A. Negi, V. S. Rana, D. S. Kathait, H. Painuly, "Compressive Behavior of Aluminum Foam Prepared by Melts Route Method by Different Addition of Nickel Particles", International Journal of Mathematics and Physical Sciences Research, Vol. 3, Issue 1, pp. 1-8, 2015.
[10] L. J. Gibson, "Mechanical Behavior of Metallic Foams", Annual Review of Materials Science, Vol. 30, pp. 191-227, 2000. https://doi.org/10.1146/annurev.matsci.30.1.191
[11] C. Motaz and R. Pippan, "Fracture behavior and fracture toughness of ductile closed-cell metallic foams", Acta Materialia, Vol. 50, Issue 8, pp. 2013-2033, 2002. https://doi.org/10.1016/S1359-6454(02)00047-2
[12] ASTM E8M Standard Test Method for Tensile Testing of Metallic Materials.
[13] O. Smorygo, A. Vazhnova and V. Mikutski, "Comparison of Mechanical Strength of Metal Foams with Different Cellular Structures and Compositions", European Powder Metallurgy Association (EPMA), 2019.
[14] J. Fan, J. Zhang, Z. Wang, Z. Li and L. Zhao, "Dynamic crushing behavior of random and functionally graded metal hollow sphere foams", Materials Science and Engineering: A, Vol. 561, pp. 352-361, 2013. https://doi.org/10.1016/j.msea.2012.10.026